

U-Net Super-Resolution Model of GOI to GOI-II Image Conversion

Jisun Shin¹, Member, IEEE, Young-Heon Jo¹, Boo-Keun Khim, and Soo Mee Kim¹, Member, IEEE

Abstract—The use of ocean color sensors presents limitations to monitoring coastal environmental changes and capturing fine spatial features below 1 km due to low spatial (0.5–1 km) and temporal (1 day) resolutions. The geostationary ocean color imager (GOI)-II, launched on February 18, 2020, is a follow-up mission to GOI, operated from June 27, 2010 to March 31, 2021. GOI-II imagery, with a spatial resolution of 250 m, detects more detailed spatial structures of ocean dynamics compared to GOI with a spatial resolution of 500 m. This study aims to develop a U-Net super-resolution (SR) model to enhance the GOI remote-sensing reflectance (R_{rs}) imagery to the same spatial resolution as GOI-II. The U-Net model is trained with eight paired bands (412, 443, 490, 555, 660, 680, 745, and 865 nm) of GOI and GOI-II R_{rs} around the waters of the Korean Peninsula. The consistency level between GOI and GOI-II images indicated GOI sensor degradation, especially in the blue bands, during its last mission period from December 2020 to March 2021. Through quantitative and qualitative evaluations, we found that the U-Net R_{rs} image had greater spectral information with higher consistency compared to the G1-bicubic image by bicubic interpolation of GOI. In particular, the U-Net results improved the consistency in the blue bands (412, 443, and 490 nm). Qualitative evaluations also showed that U-Net corrected the blue band underestimation in degraded GOI images. In addition, chlorophyll-a concentration (CHL) map from the U-Net R_{rs} not only simulated spatial patterns, similar to GOI-II CHL map, but also corrected the overestimated GOI CHL map. The U-Net SR model may help to produce more reliable and fine-scale R_{rs} products from GOI similar to those of GOI-II, and to enable long-term ocean color monitoring around the waters of the Korean Peninsula.

Index Terms—Deep U-Net super-resolution (SR) model, geostationary ocean color imager (GOI), GOI-II.

I. INTRODUCTION

OCEAN color remote-sensing data have been widely used for short- and long-term monitoring of water quality [1],

Manuscript received 30 August 2023; revised 3 January 2024 and 24 January 2024; accepted 31 January 2024. Date of publication 7 February 2024; date of current version 14 February 2024. This work was supported by the National Research Foundation of Korea (NRF) funded by the Korean Government (MSIT) under Grant NRF-2021R1A2C2006682 and Grant RS-2023-00274972. (Corresponding author: Soo Mee Kim.)

Jisun Shin is with the BK21 School of Earth and Environmental System, Pusan National University, Busan 46241, South Korea (e-mail: sj1008@pusan.ac.kr).

Young-Heon Jo and Boo-Keun Khim are with the BK21 School of Earth and Environmental System, Department of Oceanography, and Marine Research Institute, Pusan National University, Busan 46241, South Korea (e-mail: joyoung@pusan.ac.kr; bkkhim@pusan.ac.kr).

Soo Mee Kim is with the Maritime ICT and Mobility Research Department, Korea Institute of Ocean Science and Technology, Busan 49111, South Korea (e-mail: smeekim@kiost.ac.kr).

Digital Object Identifier 10.1109/TGRS.2024.3361854

[2], [3], [4], ocean productivity [5], ocean fronts [6], and blooms such as red [7], [8], [9], green, and golden tide blooms [10], [11], [12]. Monitoring and assessing water changes are carried out using ocean color sensors such as the moderate resolution imaging spectroradiometer (MODIS; Terra:1999–present; Aqua:2002–present), sea-viewing wide field-of-view sensor (SeaWiFS; 1997–2010), visible infrared imager radiometer suite (VIIRS; 2012–present), medium resolution imaging spectrometer (MERIS; 2002–2012), geostationary ocean color imager (GOI; 2010–2021), and ocean and land color instrument (OLCI; 2016–present).

GOI is the world's first ocean color sensor, operated in geostationary orbit from June 27, 2010 to March 31, 2021 [13]. GOI has a spatial resolution of 500 m and covers the Korean coastal waters, the Yellow Sea (YS), and the East China Sea (ECS). GOI specializes in monitoring hourly variations in ocean color products, with high temporal capability allowing ocean color sensors to overcome the limitations caused by frequent cloud cover. GOI has been used for many studies including the spatiotemporal variation of coastal water turbidity [14], [15], diurnal changes in red tide blooms [16], [17], [18], tracing floating green algae blooms [19], variation of sea surface salinity [20], and diurnal variation in ocean properties [21]. Park et al. [22] investigated the spatial scale of mesoscale eddies using GOI-derived chlorophyll-a concentration (CHL) products from the East Sea. Subsequently, they suggested that the fine spatial resolution of image data would allow us to identify more detailed mechanisms of ocean dynamics, including currents, mixing, air-sea interactions, and eddy-wave-current interactions. Shin et al. [7] confirmed the synergistic effect of multisensor data on red tide bloom detection along the southern coast of Korea using GOI and terrestrial sensors. They identified the differences between red tide patches extracted from GOI and terrestrial sensors with high spatial resolution. Compared to the red tide patch from GOI, the red tide patch extracted from terrestrial sensor was spatially more detailed and had sharper patterns, providing a more accurate expression of the red tide bloom.

Ocean color sensors such as MODIS (1 km of spatial resolution), VIIRS (750 m), and GOI (500 m) are limited to monitoring the coast and capturing fine spatial signals below 1 km in waters because of their low spatial resolution. In contrast, a spatial resolution of 300 m is sufficient to recognize fluctuating oceanic environment along the coast or estuary, which is particularly suitable for the Korean

Peninsula waters with complex shorelines. OLCI imagery onboard Sentinel-3A and 3B had a spatial resolution of 300 m [23]. Neckel et al. [24] reported that OLCI is efficient for the geospatial analysis of suspended sediments in terrestrial marine estuaries. Shin et al. [9] suggested that OLCI is effective for monitoring red tide blooms off the Korean coast because the Korean Peninsula has complex coastlines and numerous islands. Geostationary KOMPSAT 2B (GK2B) GOCI-II, launched on February 18, 2020, is the successor to the GOCI mission. The GOCI-II mission is expected to last ten years. If the GOCI-II mission is completed, it will allow short- and long-term monitoring of complex bio-optical waters near the East Asian region from 2010 to 2030 with the accumulated GOCI imagery. GOCI-II (250 m), which has a higher spatial resolution of four times than GOCI (500 m), allows detailed ocean signals and coastal and estuarine recognition around the Korean Peninsula. Because GOCI-II began acquiring imagery in early 2021, fine-scale monitoring is not available for previous years. If the spatial resolution of GOCI data can be improved to the level of GOCI-II, fine-scale short- and long-term monitoring data will be available from 2010 when GOCI data began to be available.

We used an image super-resolution (SR) approach based on deep learning to convert images from GOCI to GOCI-II. SR refers to the recovery of high-resolution images from low-resolution images [25]. SR has been applied in medical imaging [26], [27], surveillance, and security [28]. SR has four categories: component substitution, multiresolution analysis, geostatistical kriging, and machine learning [29]. Recently, deep convolutional neural networks (CNNs) have been applied to single-image SR [30], [31], [32], [33]. Some studies used satellite images with multispectral bands to perform SR related to building mapping [34], spatiotemporal fusion [35], land cover mapping [36], and green tide extraction [37]. Lanaras et al. [38] developed a CNN SR model of Sentinel-2 multispectral instrument (MSI) imagery with 13 spectral bands and spatial resolutions of 10, 20, and 60 m. The images in each spectral band of lower spatial resolutions (20 and 60 m) were converted into the higher resolution (10 m). They reported that the CNN model effectively learns the features of high-resolution spatial structures that existed in MSI images with 10-m spatial resolution. Liu and Wang [39] trained and evaluated a CNN SR model which improved the spatial resolution of 750 m VIIRS in six moderate (M) bands (M1–M6, 410, 443, 486, 551, 671, and 745 nm) using the VIIRS in one (I) band (638 nm) with a spatial resolution of 375 m. Because radiances in VIIRS I- and M-bands are recorded simultaneously with the same solar-sensor viewing geometry at the same ocean conditions, and then the images in VIIRS I- and M-bands were co-registered due to the same platform, the CNN model could capture the correlations between the M- and I1-band images.

In contrast to the previous two studies [38], [39], GOCI and GOCI-II have matched wavelength bands but were acquired at different platforms and times. These factors may be significant challenges in SR processing. No studies have yet conducted SR processing on geostationary ocean color products from each different sensor. This study aims to develop a U-Net SR

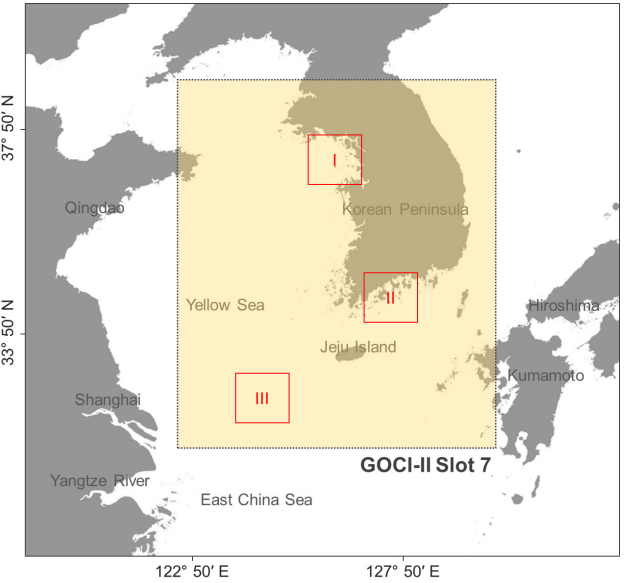


Fig. 1. Study area (black dotted box) corresponding to the scope of GOCI-II slot 7. It covers the Korean Peninsula, the YS, and the ECS. Red boxes represent the three regions chosen for validating the U-Net SR model.

model to convert images from GOCI to GOCI-II. We first evaluated the consistency of the remote-sensing reflectance (R_{rs} , sr^{-1}) GOCI and GOCI-II hourly products measured on the same dates. Second, the deep U-Net SR model was trained and evaluated using temporally paired GOCI and GOCI-II R_{rs} images in sub-regions near the coast of the Korean Peninsula. In addition, we tested whether the U-Net SR model can produce reliable ocean color products such as CHL and total suspended matter (TSM) concentration.

II. DATA AND METHODS

A. Temporally Paired GOCI and GOCI-II Datasets

Both GOCI and GOCI-II cover a 2500×2500 km 2 area around Northeast Asia, centered at 36°N and 130°E. A GOCI image comprises 16 (4 × 4) slots, while a GOCI-II image in local mode is composed of 12 (3 × 4) slots. The spatial resolutions of GOCI and GOCI-II were 500 and 250 m, respectively. GOCI and GOCI-II collect images 8 (from 0 to 7 UTC) and 10 (from 23 to 8 UTC) times per day, respectively, at hourly intervals. Of the 12 GOCI-II slots, the study area corresponding to the scope of slot seven included the area (695×695 km 2) around the Korean Peninsula, as shown in the dotted black box in Fig. 1. The study area includes the Korean Peninsula, YS, and ECS, and has the characteristics of the dynamic ocean optical properties [14], [15], [40]. We chose three regions: high turbidity waters (Region I) around Gyeonggi Bay, the waters of frequent red tide blooms (Region II) around the coast of Yeosu and Namhae, and the waters with the interaction of the ECS with Yangtze River discharge and the YS (Region III).

Fig. 2 compares the band composition and spectral response function of GOCI and GOCI-II sensors. As shown in Fig. 2(a), the spectral bands of GOCI-II correspond to the ones of GOCI at 412, 443, 490, 555, 660, 680, 745, and 865 nm except the bands at 380, 510, 620, and 709 nm. The spectral response functions of GOCI (black dotted line) and GOCI-II (red line)

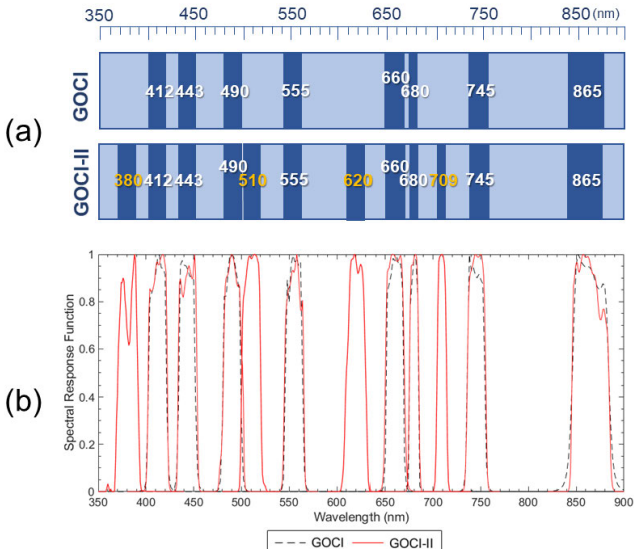


Fig. 2. (a) Band compositions and (b) spectral response functions of GOCTO and GOCTO-II.

in Fig. 2(b) exhibited similar patterns in the same wavelength bands.

In this study, we used the R_{rs} products of GOCTO and GOCTO-II after atmospheric correction to develop the SR model. The GOCTO R_{rs} product was obtained from the Korea Ocean Satellite Center (KOSC) (<https://kosc.kiost.ac.kr/>). The Korea Hydrographic and Oceanographic Agency (KHOA) provided GOCTO-II data (<https://nosc.go.kr/>). GOCTO-II Level-1 data (top-of-atmosphere radiance) were available from October 2020. GOCTO-II Level-2 data after atmospheric correction were available from December 19, 2020. GOCTO and GOCTO-II R_{rs} products are officially provided through different atmospheric correction processes. Fig. 3 shows the overlapped acquisition time zones of both GOCTO and GOCTO-II images. GOCTO and GOCTO-II images are provided 8 (0–7 UTC) and 10 \times (23–8 UTC) a day, respectively. A total of 679 paired GOCTO and GOCTO-II image data were collected from 103 overlapping acquisition days from December 19, 2020 to March 31, 2021, at 1–7 UTC at hourly intervals. During the overlapping period, the ratio of missing data was 5.83%. The missing data may be caused by station keeping, wheel of loading, and lunar observation. The final datasets were composed of 679 image pairs with eight bands at 412, 443, 490, 555, 660, 680, 745, and 865 nm of the study area (black dotted box in Fig. 1) corresponding to GOCTO-II slot 7.

We measured the consistency between 679 pairs of GOCTO and GOCTO-II R_{rs} products. To match the two images pixel-by-pixel, we converted the GOCTO images with orthographic projection into the Universal Transverse Mercator (UTM) coordinate system used by GOCTO-II. GOCTO-II images were extrapolated to the same spatial resolution (500 m) as GOCTO. First, we calculated the mean ratio of the GOCTO-II to GOCTO image pairs in each band. Next, the scatter distributions of the paired images were compared for each band. We computed the coefficient of determination (R^2), root-mean-squared error (RMSE), an unbiased percentage difference (UPD), and the mean relative difference (MRD) between GOCTO and GOCTO-II.

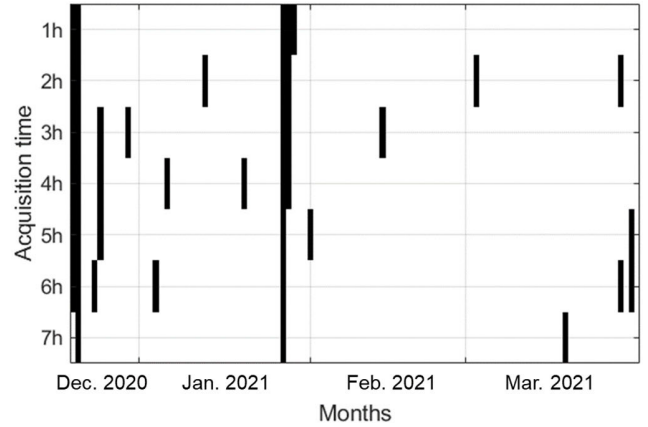


Fig. 3. Overlapped acquisition time (UTC) of both GOCTO and GOCTO-II remote-sensing reflectance (R_{rs}) images. Black box represents the missing data.

UPD and MRD are defined in the following equations:

$$\text{UPD}(\%) = \frac{1}{N} \sum_i \left| \frac{0.5(y_i - x_i)}{(y_i + x_i)} \right| \times 100 \quad (1)$$

$$\text{MRD}(\%) = \frac{1}{N} \sum_i \left[\frac{(y_i - x_i)}{x_i} \right] \times 100. \quad (2)$$

In (1) and (2), N is the number of image pairs and i represents the individual image. x and y represent GOCTO and GOCTO-II images, respectively.

B. Deep U-Net SR Model for GOCTO to GOCTO-II Conversion

A deep CNN, the U-Net model, was trained with paired GOCTO and GOCTO-II R_{rs} images as the input and output, respectively, to improve the spatial resolution of GOCTO. U-Net has a “U”-shaped CNN architecture with encoders and decoders, and is applied to pixel-wise classification or object segmentation [41]. Kim et al. [42] and Shin et al. [43] used the U-Net model to resolve the nonlinear classification of red tide blooms from the multispectral bands of the satellite images. We used the U-Net model to solve the nonlinear regression problem of GOCTO-to-GOCTO-II R_{rs} conversion. The deep convolutional layers in the U-Net extract the specific spectral features of waters from the GOCTO and GOCTO-II images. We trained the U-Net model to learn the spectral correlation and spatial enhancement between GOCTO and GOCTO-II images. Table I lists the U-Net structures, comprising an input layer, four encoder blocks, a bridge layer, four decoder blocks, and an output layer. The total number of layers is 57. Zero-centered normalization is applied to the input patches. The encoder block reduces the spatial dimension and increases the channel number to capture the specific features in GOCTO patches, and the decoder block transfers the encoded information to a higher dimension by reducing the channel number and increasing the spatial dimension. The bridge block connects the encoder and the decoder blocks. Each decoder block concatenates the features extracted from the corresponding encoding blocks. Dropout layers are added to the last encoder and bridge blocks. The adopted loss function in the regression layer is a mean-squared error (MSE).

TABLE I
DETAILED STRUCTURES OF THE U-NET SUPER-RESOLUTION MODEL FROM GOCI TO GOCI-II. THE CHANNEL NUMBER OF INPUT AND OUTPUT IMAGES IS 8

Encoder		Decoder	
Blocks	Layers per Block	Blocks	Layers per Block
Input	Input layer (128×128×8)	Output	Regression Output (128×128×8) Final-Conv (1×1)
Encoder-1 to 3	Conv (3×3)/ReLU Conv (3×3)/ReLU MaxPool (2×2)	Decoder-1 to 4	UpConv (2×2)/ReLU Depth concatenation Conv (3×3)/ReLU Conv (3×3)/ReLU
Encoder 4	Conv (3×3)/ReLU Conv (3×3)/ReLU DropOut MaxPool (2×2)	Bridge	Conv (3×3)/ReLU Conv (3×3)/ReLU DropOut

After confirming the pixel-wise consistency level between GOCI and GOCI-II, we selected 384 (80%) and 95 (20%) image pairs obtained between January 19, 2021 and March 31, 2021, for training and testing the U-Net model, respectively. GOCI images were resampled by bicubic interpolation to obtain a smaller pixel size of 250 m same as the spatial resolution of GOCI-II. We split the image pairs into spatially nonoverlapping patches of 128 × 128 × 8 pixels. To select valid training patch pairs, we performed two preprocessing steps: 1) applying the mask and 2) selecting valid patch pairs. First, after generating a mask that selects only the overlapping pixels between each patch pair for each wavelength band, we generate a common mask by pixel-wise OR logical operation of eight wavelength-dependent masks. Thereafter, a pixel pair was removed if the pixel value ratio of GOCI-II to GOCI was more than 2. We used only the corresponding patch pairs for training when the total number of remaining pixels was 10% or more in the patch pair after applying a common mask and the R² of the corresponding pixels in the patch pair was 0.5 or more. We thereby obtained 10 162 (80%) and 2541 (20%) valid patch pairs of GOCI and the corresponding GOCI-II (ground truth) for training and testing the SR model, respectively. The GOCI data were upsampled to a spatial resolution of 250 m by bicubic interpolation which is common for downsampling and upsampling. Then, we used G1-bicubic as input of the U-Net model and compared G1-bicubic with U-Net results. The U-Net model was trained for the transition from GOCI to GOCI-II by learning the pixel-wise spatial and spectral information. We trained the U-Net model using stochastic gradient descent with a momentum optimizer with ten mini-batches for 25 epochs. The hyperparameters of the L2 regularization and learning rate were set to 0.0001 and 0.05, respectively.

C. Performance Evaluation of the U-Net SR Model

To evaluate quantitatively and qualitatively the performance of the trained U-Net SR model, we compared the R_{rs} derived from the U-Net model (U-Net R_{rs}) and G1-bicubic R_{rs} with GOCI-II as the ground truth. For quantitative evaluation, we evaluate the peak signal-to-noise ratio (PSNR), structural similarity (SSIM), and entropy of each wavelength band using

a test dataset. PSNR assesses the degree of distortion of the resultant SR images from the U-Net model and bicubic interpolation in (3). A higher PSNR indicates a smaller degree of distortion between the recovered SR image and the ground-truth image

$$\text{PSNR}(x_i, y_i) = 10 \times \log_{10} \left(\frac{1}{\text{MSE}} \right) (\text{dB}) \quad (3)$$

$$\text{MSE} = \frac{1}{N} \sum_i (y_i - x_i)^2. \quad (4)$$

In (3), x represents SR images, U-Net or G1-bicubic images, and y represents GOCI-II (ground truth) image. MSE is computed between GOCI-II and the estimated SR image in (4). N is the number of image pairs and i represents the individual image.

SSIM evaluates the SSIM between the estimated SR and GOCI-II images in (5). SSIM ranges from -1 to 1. The larger the SSIM, the higher the similarity between the two images

$$\begin{aligned} \text{SSIM} &= l(x, y) \cdot c(x, y) \cdot s(x, y) \\ &= \left(\frac{2\mu_x\mu_y + C_1}{\mu_x^2 + \mu_y^2 + C_1} \right) \cdot \left(\frac{2\sigma_x\sigma_y + C_2}{\sigma_x^2 + \sigma_y^2 + C_2} \right) \\ &\quad \cdot \left(\frac{\sigma_{xy} + C_3}{\sigma_x\sigma_y + C_3} \right). \end{aligned} \quad (5)$$

In (5), $l(x, y)$, $c(x, y)$, and $s(x, y)$ are the luminance, contrast, and structure comparison functions of two images, x and y , respectively. μ_x and μ_y represent the means of x (the estimated SR image) and y (GOCI-II image). σ_x and σ_y are the standard deviations. σ_{xy} is the cross-covariance between the two images. Three constants, C_1 , C_2 , and C_3 set to 10⁻⁴, 3 × 10⁻⁴, and 1.5 × 10⁻⁴, respectively.

Entropy in (6) is a statistical measure of the randomness that characterizes the texture of an image. The greater the entropy, the greater the amount of information contained in the image. p contains the normalized histogram counts in the image

$$\text{Entropy} = - \sum p \log_2(p). \quad (6)$$

Also, we compared the consistencies at four wavelength bands (443, 490, 555, and 680 nm) between the U-Net, G1-bicubic, and GOCI-II R_{rs} in the three chosen subregions in Fig. 1. We computed the R², RMSE, UPD, and MRD and compared the spatial distribution of the GOCI-II, G1-bicubic, and U-Net R_{rs} at 443, 490, 555, and 680 nm for each subregion. We chose GOCI and GOCI-II R_{rs} products acquired on March 22, 2021, 1 h (UTC) around Gyeonggi-bay, on February 19, 2021, 3 h (UTC) around the coast of Yeosu and Namhae, and on February 20, 2021, 1 h (UTC) around the ECS.

Ocean color data, especially R_{rs} products, have helped us understand chlorophyll-a dynamics and TSM variations [4], [44], [45], [46], [47]. The CHL product from GOCI R_{rs} was estimated for the OC3 algorithm [48] in the following equations:

$$\text{CHL}_{\text{OC3}} = 10^{c_0+c_1R+c_2R^2+c_3R^3+c_4R^4} \quad (7)$$

$$R = \frac{\max[R_{\text{rs}}(443), R_{\text{rs}}(490)]}{R_{\text{rs}}(555)}. \quad (8)$$

TABLE II

MEAN AND STANDARD DEVIATION (SD) OF THE R_{rs} RATIO OF GOCI-II TO GOCI FOR EACH SPECTRAL BAND. B1, B2, B3, B4, B5, B6, B7, AND B8 REPRESENT 412, 443, 490, 555, 660, 680, 745, AND 865 nm, RESPECTIVELY

	B1	B2	B3	B4	B5	B6	B7	B8
Mean	1.62	1.45	1.18	0.78	0.91	0.89	0.93	0.94
SD	1.09	0.62	0.25	0.22	0.25	0.16	0.25	0.23

In (7), c_0 , c_1 , c_2 , c_3 , and c_4 are 0.0831, -1.9941, 0.5629, 0.2944, and -0.5458, respectively. Generally, the CHL product from GOCI-II is obtained using the OC4 algorithm with four wavelength bands at 443, 490, 510, and 555 nm. However, because GOCI does not have a 510-nm band, we used the OC3 algorithm with common bands at 443, 490, and 555 nm. The GOCI TSM product was estimated using the YS and ECS Ocean Color (YOC) algorithms [49] in the following equation:

$$TSM = 10^{b_1 + b_2(R_{rs}(555) + R_{rs}(670)) - b_3 \left(\frac{R_{rs}(490)}{R_{rs}(555)} \right)}. \quad (9)$$

In (9), b_1 , b_2 , and b_3 are 0.649, 25.623, and 0.646, respectively. We adjusted the wavelength band from 670 to 680 nm to calculate the TSM. Unlike the GOCI TSM map, the standard TSM algorithm with GOCI-II utilizes the spectral images at 620 nm. The OC3 and YOC algorithms were applied to GOCI-II (ground truth), GOCI, G1-bicubic, and U-Net R_{rs} products. We compared the spatial distributions and patterns of the CHL and TSM maps estimated from the four products.

III. RESULTS

A. Spectral Consistency Between GOCI and GOCI-II

To identify spectral consistency between GOCI and GOCI-II, we measured the R_{rs} ratio of GOCI-II to GOCI images on the same day as shown in the scatter distributions (Fig. 4) and the mean and standard deviation (Table II). Fig. 4 shows the ratio of GOCI-II to GOCI R_{rs} products for each wavelength band of the 679 image pairs. In the blue wavelength bands (412–490 nm), the ratio was significantly higher than 1. The ratio of the 490 nm band was the closest to 1, while the 412-nm band with shortest wavelength showed the highest ratio [Fig. 4(a)]. In particular, the ratio of the 412-nm band before the 200th order of image pairs was up to 7.07. After the 400th order of image pairs, all three blue bands showed slightly greater ratios than 1. The green band (555 nm) exhibited a ratio below 1 [Fig. 4(b)]. For the red (660 and 680 nm) and near-infrared (NIR, 745 and 865 nm) bands, after the 200th order of image, the calculated ratios were relatively close to 1. Table II lists the mean and standard deviation (SD) of the calculated GOCI-II to GOCI R_{rs} ratio for each spectral band. Within the blue wavelength bands, the shorter the wavelength, the larger the mean and SD values of the ratio. The mean ratio in the green band tended to be slightly underestimated, as it had the lowest mean value among all the bands, with an SD of 0.22. In the red and NIR bands, the mean value of the R_{rs} ratio showed a stable ratio of approximately 0.9, and SDs were 0.16–0.25, which was not in a large range.

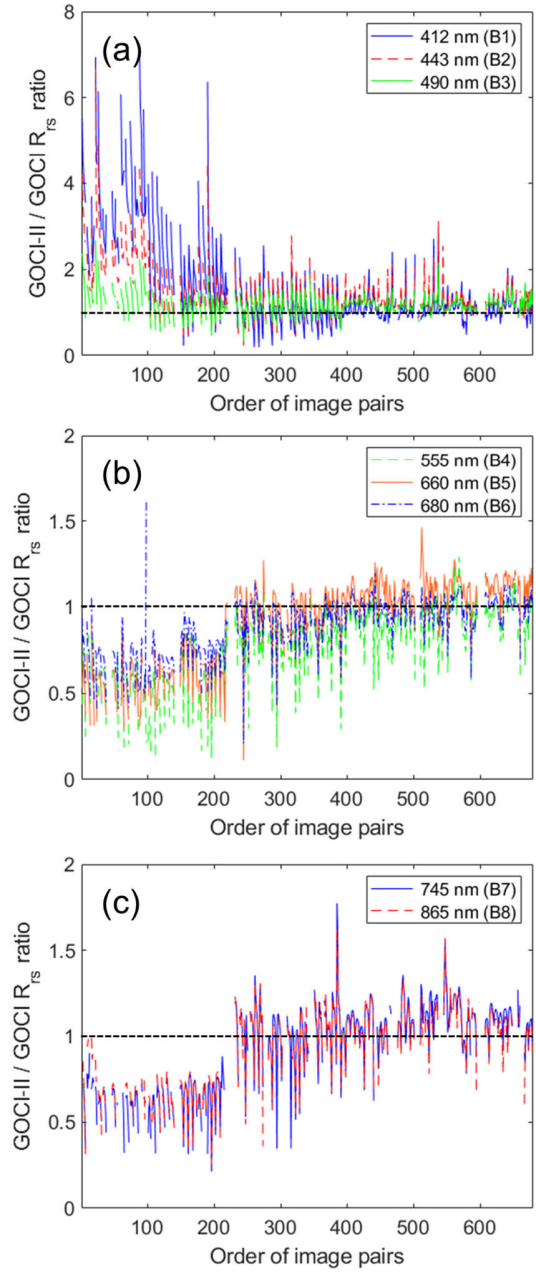


Fig. 4. R_{rs} ratio of GOCI-II to GOCI. (a) Blue wavelength bands of 412, 443, and 490 nm. (b) Green (555 nm) and red bands (660 and 680 nm). (c) Near-infrared (NIR, 745 and 865 nm) bands. The x -axis represents the order of image pairs. Black dotted lines indicate the ratio between GOCI-II and GOCI R_{rs} of 1.

The smallest SD level among the bands was observed for the red band (660 nm).

Fig. 5 shows the R_{rs} scatterplots of GOCI-II (x -axis) and GOCI (y -axis) for each spectral band. Consistency patterns can be visualized between the GOCI and GOCI-II R_{rs} for the eight wavelengths. Red (660 and 680 nm) and blue (412 and 443 nm) wavelengths showed the best and worst consistencies, respectively. The statistical comparison results are summarized in Table III. In terms of R^2 and RMSE, the 680-nm band showed the highest consistency with 0.95 and 0.0008 sr^{-1} , whereas the 412-nm band ($R^2 = 0.33$, $\text{RMSE} = 0.0053 \text{ sr}^{-1}$) had the lowest consistency among the eight bands. UPD showed the lowest (5.29%) and highest (9.59%) values

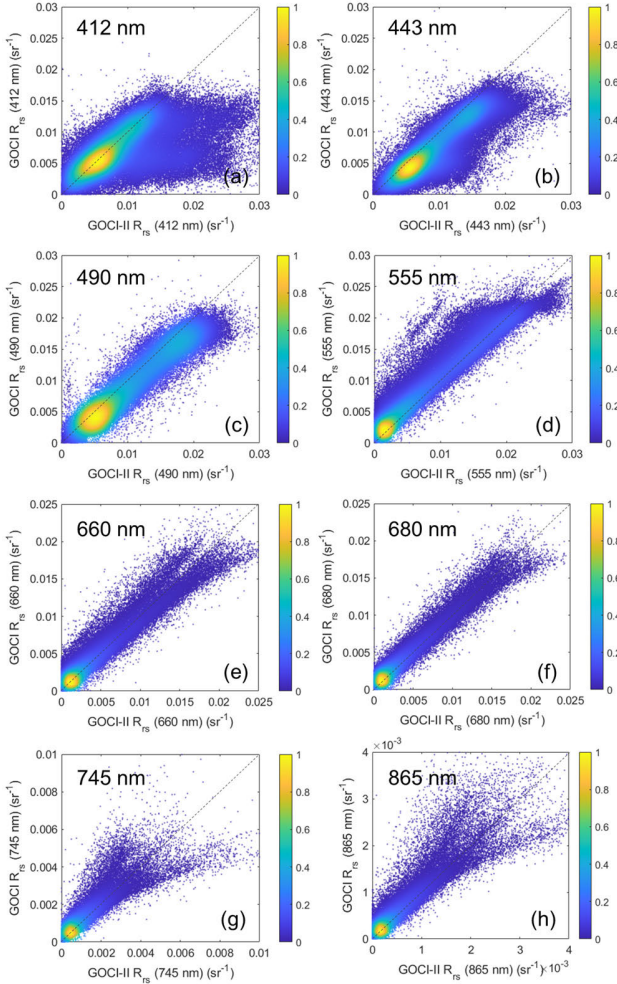


Fig. 5. R_{rs} scatterplots of GOCT-II (x-axis) and GOCT (y-axis) for each spectral band. (a) 412, (b) 443, (c) 490, (d) 555, (e) 660, (f) 680, (g) 745, and (h) 865 nm.

TABLE III

PIXEL PAIR NUMBER (N), COEFFICIENT OF DETERMINATION (R^2), RMSE, AND UPD, AND THE MRD BETWEEN GOCT-II AND GOCT R_{rs}

	N	R^2	RMSE (sr $^{-1}$)	UPD (%)	MRD (%)
B1 (412 nm)	154,641	0.33	0.0053	9.59	60.49
B2 (443 nm)	159,367	0.74	0.0032	7.99	68.49
B3 (490 nm)	162,008	0.93	0.0021	5.29	30.02
B4 (555 nm)	134,944	0.91	0.0023	7.04	-14.43
B5 (660 nm)	142,276	0.93	0.0012	7.11	10.37
B6 (680 nm)	152,332	0.95	0.0008	7.76	-9.22
B7 (745 nm)	134,056	0.82	0.0004	7.64	4.54
B8 (865 nm)	133,944	0.85	0.0002	7.75	8.27

at 490 and 412 nm, respectively. The minimum (4.45%) and maximum (68.49%) MRDs were at 745 and 443 nm, respectively. Through the statistical results in Section III-A, we found that GOCT R_{rs} values in the blue wavelength bands (especially in the 412 nm) were underestimated compared to GOCT-II R_{rs} values. In the green wavelength bands, GOCT R_{rs} was slightly overestimated compared with GOCT-II R_{rs} , whereas the paired R_{rs} generally matched in the red wavelength bands. In the case of NIR wavelength bands, the degree of agreement between GOCT and GOCT-II increased significantly as the R_{rs} values increased.

TABLE IV
PSNR, SSIM, AND ENTROPY OF G1-BICUBIC AND U-NET MODEL USING THE TEST DATASET OF THE ENTIRE REGION. B1, B2, B3, B4, B5, B6, B7, AND B8 REPRESENT 412, 443, 490, 555, 660, 680, 745, AND 865 NM, RESPECTIVELY

	G1-Bicubic			U-Net model		
	PSNR	SSIM	Entropy	PSNR	SSIM	Entropy
B1	53.94	0.9847	1.87	54.40	0.9858	1.87
B2	53.08	0.9840	1.99	56.84	0.9940	2.09
B3	54.40	0.9907	2.19	58.35	0.9964	2.34
B4	57.45	0.9947	2.61	57.72	0.9949	2.63
B5	60.71	0.9971	1.80	62.36	0.9980	1.86
B6	62.46	0.9977	1.69	63.48	0.9983	1.68
B7	68.27	0.9992	0.43	68.88	0.9993	0.51
B8	73.94	0.9997	0.13	71.75	0.9995	0.20

B. Performance of the U-Net SR Model

Table IV summarizes the PSNR, SSIM, and entropy of G1-bicubic and U-Net R_{rs} for the eight corresponding bands of GOCT and GOCT-II using the test dataset. Except for the B8 band (865 nm), the PSNR of the U-Net R_{rs} was higher than that of the G1-bicubic. The PSNRs of both G1-bicubic and U-Net R_{rs} tended to decrease as the wavelength increased from B1 (412 nm) to B8 (865 nm). The mean PSNRs of the G1-bicubic and U-Net R_{rs} with all bands are 60.53 and 61.72 dB, respectively. In the blue bands (412–490 nm), the G1-bicubic and U-Net R_{rs} exhibited mean PSNR of 53.81 and 56.53, respectively. This indicates that the U-Net R_{rs} had a smaller distortion than the G1-bicubic in the blue bands compared to GOCT-II. The SSIM of both models for all bands was close to 1 and the mean SSIM of the U-Net R_{rs} (0.9958) was slightly higher than G1-bicubic (0.9935) for all bands. The U-Net R_{rs} has a higher entropy level than the G1-bicubic for all bands. We confirmed that the R_{rs} image estimated using the U-Net model represented spectral information closer to the ground-truth GOCT-II than to the G1-bicubic.

Table V compares the consistencies in terms of R^2 , RMSE, UPD, and MRD between the estimated R_{rs} product from G1-bicubic and the U-Net models and the reference GOCT-II R_{rs} in subregions I–III of Fig. 1. The R^2 for the G1-bicubic and U-Net R_{rs} were similar. However, the other statistical indices showed improvements in U-Net R_{rs} compared to G1-bicubic. Compared with G1-bicubic, the average RMSE over the four bands (B2, B3, B4, and B6) of U-Net decreased by 17.33%, 20.31%, and 34.40% in subregion I–III, and the average UPDs of U-Net R_{rs} also decreased by 22.97%, 28.07%, and 47.98% in subregion I–III, respectively. The degrees of improvement in the average RMSE and UPD were greatest in Region III and smallest in Region I. The waters of Region III had no significant spatiotemporal fluctuations in CHL and TSM maps, compared to Regions I and II. The U-Net model shows the highest degree of improvement in all regions at the two blue bands (443 and 490 nm) compared to the 555 nm and 680 nm bands. In contrast, the RMSEs and UPDs of U-Net at the B4 (555 nm) and B6 (680 nm) bands tended to be slightly worse than those of G1-bicubic in Region I. Compared to G1-bicubic, the MRD of the U-Net model showed a noticeable improvement in the 412-nm band in the three subregions,

TABLE V

R^2 , RMSE, UPD, AND MRD OF G1-BICUBIC AND U-NET MODELS REFERENCE THE GOCI-II TEST DATASET IN THE THREE SUBREGIONS. R1, R2, AND R3 REPRESENT REGIONS I–III, RESPECTIVELY, AS IN FIG. 1. B2, B3, B4, AND B6 REPRESENT 443, 490, 555, AND 680 nm, RESPECTIVELY

Region	SR Model	Band	R^2	RMSE (sr^{-1})	UPD	MRD
R1	G1-Bicubic	B2	0.44	0.0022	6.08	28.01
		B3	0.52	0.0022	4.82	20.53
		B4	0.39	0.0018	3.27	5.94
		B6	0.94	0.0013	3.69	16.12
	U-Net	B2	0.46	0.0014	2.89	4.22
		B3	0.55	0.0013	2.46	7.97
		B4	0.40	0.0019	3.69	8.39
		B6	0.92	0.0016	4.71	21.27
R2	G1-Bicubic	B2	0.63	0.0022	4.52	19.03
		B3	0.67	0.0022	3.97	17.12
		B4	0.69	0.0015	2.49	1.98
		B6	0.85	0.0007	4.99	-10.64
	U-Net	B2	0.59	0.0015	2.48	4.37
		B3	0.65	0.0017	2.51	8.88
		B4	0.70	0.0015	2.83	4.03
		B6	0.87	0.0006	3.67	-4.05
R3	G1-Bicubic	B2	0.49	0.0022	4.12	16.65
		B3	0.76	0.0023	3.22	13.53
		B4	0.60	0.0025	2.66	10.46
		B6	0.82	0.0016	2.69	11.84
	U-Net	B2	0.57	0.0007	0.87	1.94
		B3	0.68	0.0009	1.01	3.22
		B4	0.59	0.0025	2.72	10.90
		B6	0.82	0.0014	2.01	8.14

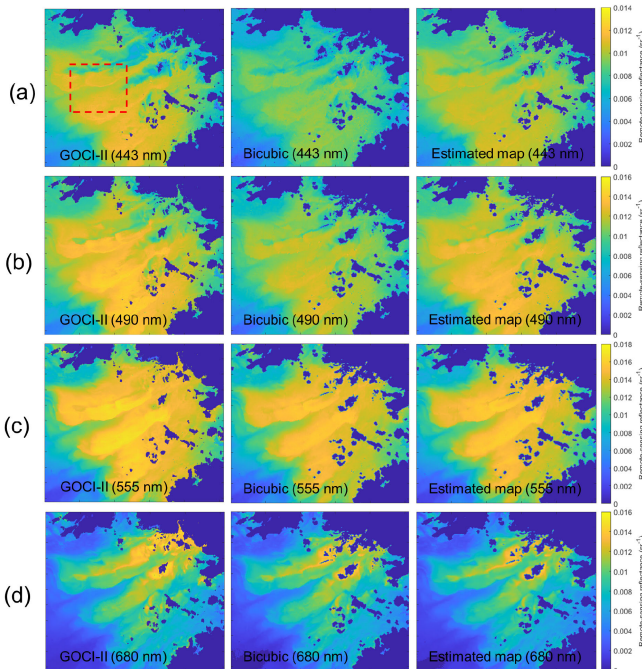


Fig. 6. R_{rs} maps of GOCI-II (left column), G1-bicubic (middle column), and U-Net model (right column) at (a) 443, (b) 490, (c) 555, and (d) 680 nm bands. The images were acquired on March 22, 2021, 1 h (UTC) around Gyeonggi-bay in Region I of Fig. 1. The red dotted square of (a) represents the area for CHL and TSM concentration map.

by 84.93%, 77.02%, and 88.35%, respectively. This indicates that our U-Net model overcomes the underestimation tendency of the G1-bicubic model.

In accordance with Table V, Figs. 6–8 compare the spatial distributions of the R_{rs} product at the B2, B3, B4, and B6 (443,

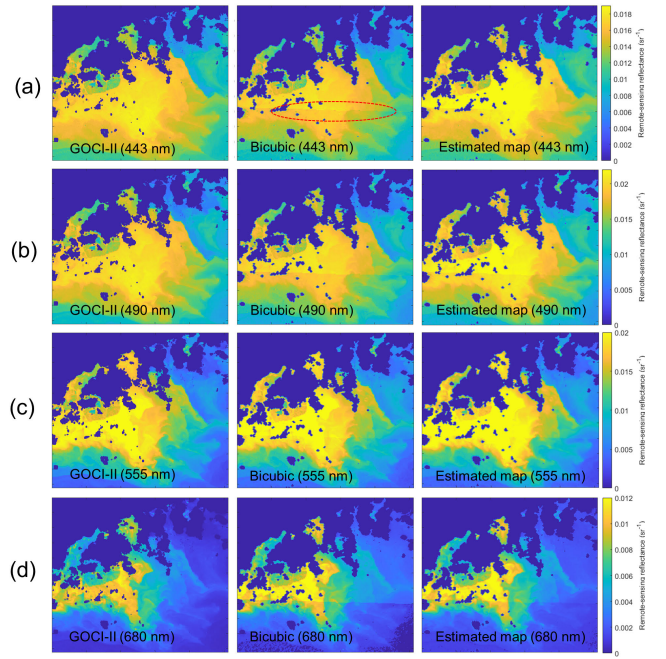


Fig. 7. R_{rs} maps of GOCI-II (left column), G1-bicubic (middle column), and U-Net model (right column) at (a) 443, (b) 490, (c) 555, and (d) 680 nm bands. The images were acquired on February 19, 2021, 3 h (UTC) around the coast of Yeosu and Namhae as shown in Region II of Fig. 1. The red dotted ellipse represents the slot boundary.

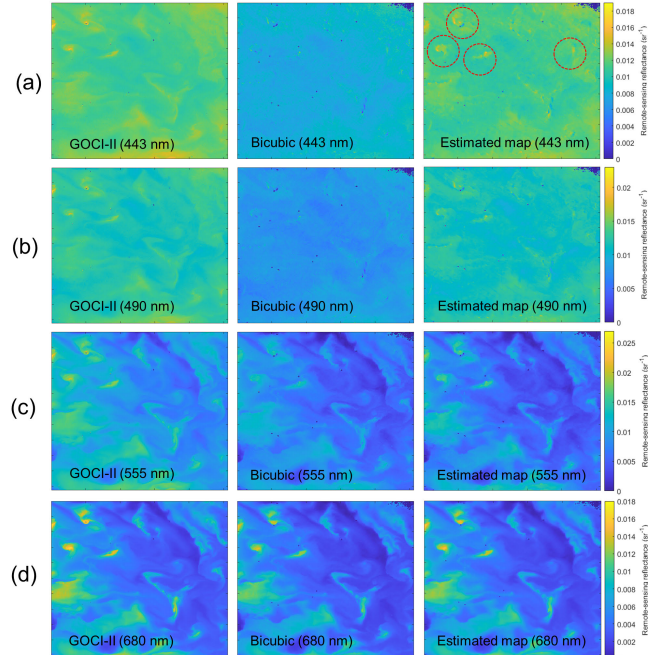


Fig. 8. R_{rs} maps of GOCI-II (left column), G1-bicubic (middle column), and U-Net model (right column) at (a) 443, (b) 490, (c) 555, and (d) 680 nm bands. The images were acquired on February 20, 2021, 1 h (UTC) around the ECS as shown in Region III of Fig. 1. The red dotted circles represent the ocean current patterns.

490, 555, and 680 nm) bands of GOCI-II, G1-bicubic, and U-Net models in Regions I–III. As shown in Fig. 6, the blue wavelength band of the G1-bicubic R_{rs} images (especially at 443 nm band) showed a typical spatial pattern in the estuary of Gyeonggi Bay, with R_{rs} value underestimated compared

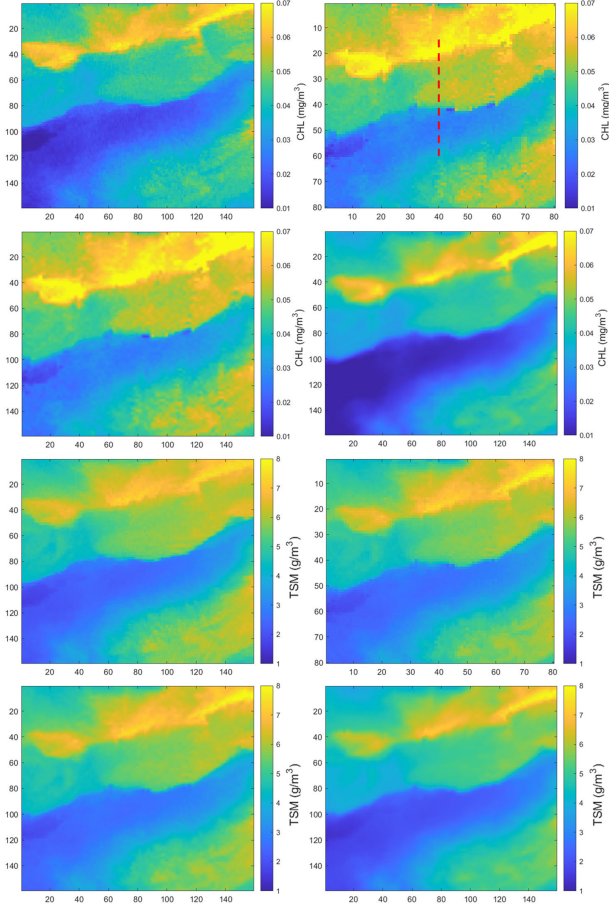


Fig. 9. CHL and TSM maps. All maps enlarged the red dot square in Fig. 6(a). (a) GOCI-II CHL, (b) GOCI CHL, (c) G1-bicubic CHL, (d) U-Net CHL, (e) GOCI-II TSM, (f) GOCI TSM, (g) G1-bicubic TSM, and (h) U-Net TSM maps. The red dotted line of (b) represents the selected line for plots of CHL and TSM.

to that of GOCI-II R_{rs} (ground-truth). By contrast, the blue-band R_{rs} images derived from our U-Net model showed significant improvement on the underestimation tendency in the G1-bicubic image. In Region II, the U-Net model results showed similar improvements to Region I (Fig. 7). Characteristically, we found that the slot boundary across the coastal waters seen in the GOCI map was still visible in the G1-bicubic map as shown in Fig. 7(a), whereas the slot boundaries disappeared in our U-Net model results. In Fig. 8, compared to GOCI-II, the ocean current pattern in the ECS of Region III was not well revealed in the 443-nm band of the G1-bicubic image, but a noticeable pattern appeared on the U-Net R_{rs} map. For both the 555- and 680-nm band images, both the G1-bicubic and U-Net R_{rs} maps showed similar spatial patterns and R_{rs} levels to the GOCI-II R_{rs} images.

We tested the dependency of the SR model on the estimation of the CHL and TSM maps at a resolved spatial scale (250 m). Fig. 9 compares the CHL and TSM maps estimated from the GOCI, GOCI-II (ground-truth), G1-bicubic, and U-Net R_{rs} images in the region indicated by the red dotted square in Fig. 6(a). Compared to the ground truth, GOCI-II, with a 250-m spatial resolution, we found pixel-wise

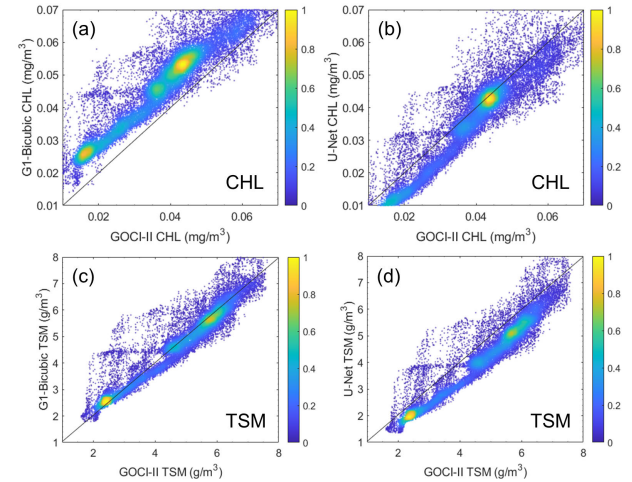


Fig. 10. Scatterplots. (a) G1-bicubic versus GOCI-II CHL maps. (b) U-Net versus GOCI-II CHL maps. (c) G1-bicubic versus GOCI-II TSM maps. (d) U-Net versus GOCI-II TSM maps.

TABLE VI
 R^2 , RMSE, UPD, AND MRD OF G1-BICUBIC AND U-NET MODELS
 WITH THE REFERENCE OF GOCI-II CHL AND TSM

	R^2	RMSE	UPD (%)	MRD (%)
G1-Bicubic CHL	0.85	0.01 mg m ⁻³	6.36	-21.61
U-Net CHL	0.86	0.006 mg m ⁻³	4.35	14.54
G1-Bicubic TSM	0.91	0.45 g m ⁻³	1.73	-0.22
U-Net TSM	0.91	0.67 g m ⁻³	3.71	13.91

cascaded patterns in GOCI (500-m spatial resolution) and G1-bicubic CHL and TSM maps, especially near the boundaries of different seawater types. In particular, the GOCI and G1-bicubic CHL maps showed significantly overestimated spatial patterns compared to the GOCI-II CHL map, whereas U-Net CHL showed a similar spatial pattern to the GOCI-II CHL map. In the case of the TSM maps, all GOCI, G1-bicubic, and U-Net TSM showed spatial patterns similar to the GOCI-II TSM, except that the U-Net TSM map tended to be slightly underestimated compared to the GOCI-II TSM.

We compared quantitatively the degree of agreement between CHLs and TSMs (Fig. 9) of the SR predictions and GOCI-II in Fig. 10 and Table VI. Fig. 10 compares the consistency between the CHL and TSM maps estimated from the G1-bicubic, U-Net, and GOCI-II R_{rs} . In Fig. 10(a) and (b), the G1-bicubic CHL showed a biased consistency, whereas the U-Net CHL map matched better with the GOCI-II CHL. As shown in Table VI, the R^2 levels in the two scatterplots of G1-bicubic and U-Net were similar, but the RMSE and UPD of the U-Net CHL map were reduced by 40% and 31.6% compared to the G1-bicubic CHL map, respectively. The MRD level was overestimated in the G1-bicubic CHL (-21.61%) but slightly underestimated in the U-Net CHL (14.54%). The consistency of the TSM map was similar in terms of the R_{rs} for the two scatterplots [Fig. 10(c) and (d)]; however, there was no significant improvement in the other index levels. As shown in Table V, B4 and B6 bands of the G1-bicubic showed a higher degree of agreement to the ground truth (GOCI-II) than the U-Net,

especially at 680 nm. Since the TSM algorithm utilizes a 680-nm band as in (9), it is believed the TSM retrial result was derived due to the difference in R_{rs} agreement between G1-bicubic and U-Net.

IV. DISCUSSIONS

A. Discrepancy Between GOCHI and GOCHI-II

For reliable long-term monitoring, the spectral consistency and the temporal continuity between sensors must be guaranteed. In this study, we assessed the R_{rs} ratio and scatter distribution between the GOCHI-II and GOCHI R_{rs} products. We found that the consistency was lower in the blue wavelength bands than in the other bands. The same phenomenon has been reported in previous studies. Hu and Le [50] reported the worst consistency at 443 nm and the unique patterns in the spatial distribution of R_{rs} differences at 443 and 486 nm between MODIS and VIIRS data. Park et al. [1] reported a lower consistency at 443 and 490 nm of GOCHI R_{rs} from 2012 to 2021 than at 555-nm band compared with MODIS, and VIIRS. In addition, they mentioned the sensor degradation of GOCHI during the late mission period (2019–2021). The lower consistency of the blue bands, especially at the 412-nm band ($R^2 = 0.33$, MRD = 60.49%) is related to separate atmospheric corrections. In particular, our study area, particularly Region I, was rich in CHL, TSM, and CDOM, leading to a low R_{rs} magnitude and high absorption in the blue band, and increased R_{rs} uncertainty. As shown in Fig. 3, the GOCHI data from December 2020 to January 2021 were affected by the sensor degradation. The local mode of GOCHI-II was observed by dividing the central area of the Korean Peninsula into 12 slots, while that of GOCHI was divided into 16 slots. Both sensors had an observation time of 15–45 min/h. The exposure time of two sensors varied within approximately 70 s depending on the observation plan for each slot even in the same area and the different observation times may reduce the consistency between images. The interslot radiometric discrepancy (ISRD) of GOCHI [51] varied irregularly according to the image and the time zone and it was generally noticeable in the blue wavelength band. The GOCHI-II image avoids the influence of the ISRD by placing the area around the Korean Peninsula in one slot. Accordingly, the GOCHI ISRD phenomenon may be a factor that lowers the consistency between the two sensors.

B. Uncertainty of U-Net R_{rs} Product

We trained the U-Net model with GOCHI and the corresponding GOCHI-II R_{rs} at eight bands as the input and output, respectively. Our model aimed to enhance spatial resolution and to learn spectral features of ocean color imageries measured from sensors in different platforms. In this study, we recognized that the performance of the U-Net model varied according to the specific region and wavelength band. When the U-Net was tested with images obtained in three sub-regions having different optical properties, the performance in Region III had lower RMSE, UPD, and MRD values than those in Regions I and II. Because

Region III is a part of the ECS with less complex optical properties than Regions I and II, the SR process results in fewer errors in Region III. In fact, we confirmed whether model performance was improved by adding patch pairs reflecting the complex optical properties of Region I, but we could not perform because there were not many patch pairs obtained after pre-processing in 679 images due to significant masking by cloud. Thus, we focused on developing a model targeting various optical properties rather than a specific model for Region I. In addition, model performance in Regions II and III was relatively higher than that of Region I, but as shown in Table V, the performance in Region I is reasonable. In terms of model performance by band, the blue bands exhibited lower performance than the other bands in both quantitative evaluations. These results are similar to those reported by Liu and Wang [39]. They trained the CNN model to convert 750-m spatial resolution VIIRS data to 375 m. They noted that the result at 443 nm in the Baltic Sea band was more widespread than those at 551 and 671 nm. In addition, the standard deviation between the super-resolved and original data increases as the wavelength decreases from 486 to 410 nm. However, the data points of the Bohai Sea model are much closer to the 1:1 line than those of the Baltic Sea model. They reported that the images in the Bohai Sea were much smoother and contained fewer fine spatial features than those in the Baltic Sea.

The discrepancy between image pairs used to train the model mentioned in the previous section may be the most significant factor in lowering model performance. The U-Net model was trained by setting the patch size to 128×128 pixels. Each patch had an area of 32×32 km = 1024 km^2 , consisting of 16 patches for each region. We trained the model with patches of different sizes (e.g., 64×64 or 256×256), and then we chose the patch size with 128×128 pixels exhibiting the best quantitative performance and more accurate spatial patterns of the R_{rs} . Also, we initially trained the U-Net model that converted GOCHI with the original resolution (500 m) to GOCHI-II (250 m), but it was not well trained. Hence, we chose the U-Net model converting G1-bicubic (250 m) to GOCHI-II (250 m). In the convolution layer of U-Net, the padding option is set to “symmetric-include-edge” to avoid the artifacts on the edge of the patch image. All of these factors may affect the performance of the U-Net model.

C. Improved Consistency of CHL and TSM Maps

We evaluated the dependency of the U-Net model on three regions having different optical properties of the waters and observed CHL and TSM fluctuations in Region I. In general, estuaries are greatly affected by human activities and climate change, which can be recognized by the changes in TSM and CHL [52], [53]. Gyeonggi Bay (Region I) is one of the most widely developed estuaries on the coast of the Korean Peninsula, and it is important to monitor coastal environmental changes through TSM and CHL maps. These waters usually have TSM in the range of $0\text{--}10 \text{ g/m}^3$ in general and TSM

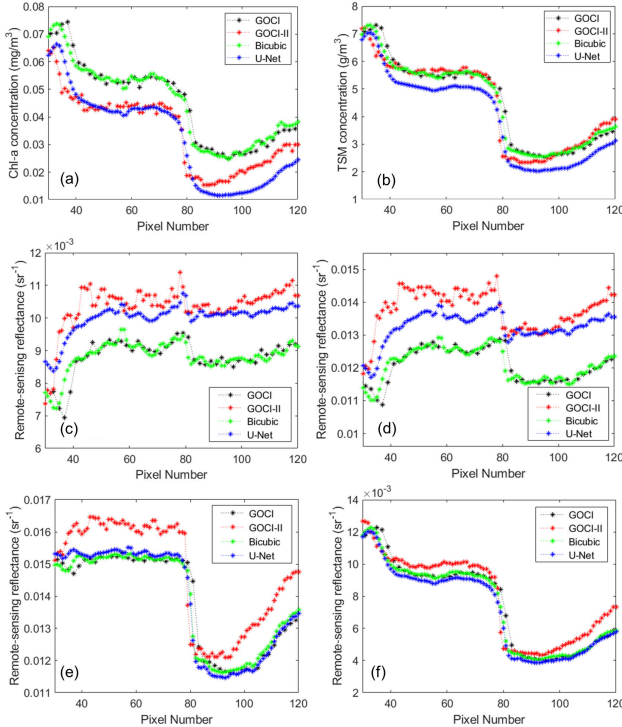


Fig. 11. Plots of (a) CHL, (b) TSM, and R_{rs} at (c) 443 nm, (d) 490 nm, (e) 555 nm, and (f) 680 nm along the red dotted line in Fig. 8(a) in GOCI (black dotted line), GOCI-II (red dotted line), G1-bicubic (green dotted line), and U-Net (blue dotted line) images.

varies more than 20 g/m^3 depending on the tidal cycle [54]. The monitoring of spatially detailed TSM or CHL fluctuations along the estuary coast is limited at a spatial resolution of 500 m. As shown in Fig. 9, the U-Net CHL and TSM maps expressed ocean current patterns with fine scales better than those of G1-bicubic. The overestimation pattern shown in the GOCI and G1-bicubic CHL maps completely disappeared in the U-Net CHL map. Fig. 11(a) and (b) compared the plots extracted from GOCI, GOCI-II, G1-bicubic, and U-Net CHL and TSM maps along the selected line in Fig. 9(b). We found that GOCI products were much smoother than GOCI-II, G1-bicubic, and U-Net products. GOCI and G1-bicubic CHL levels were generally overestimated, whereas it is observed similar values and patterns in GOCI-II and U-Net CHLs. All TSM maps showed similar patterns and values. These results were related to the R_{rs} bands used in the CHL and TSM algorithms. Chlorophyll has absorption wavelengths of 443, 490, and 510 nm and fluorescence properties in the 680 nm. The higher the TSM, the higher the scattering and absorption of floating particles, which increases the value of the 555-nm band. As shown in Fig. 11(c) and (d), GOCI and G1-bicubic R_{rs} at 443 and 490 nm were underestimated compared with GOCI-II and U-Net R_{rs} . In fact, at $R_{rs} = 555 \text{ nm}$, the U-Net R_{rs} was estimated to be similar to GOCI and G1-bicubic R_{rs} . Our results showed that the consistency level of GOCI and G1-bicubic CHL products is lower owing to the low consistency of the estimated R_{rs} in the blue band. This may be not only due to the GOCI sensor degradation during its last mission period but also the common issue of inaccurate atmospheric correction in the blue band for all ocean color

sensors. Our U-Net model allows us to reliably estimate CHL by increasing the consistency of the R_{rs} product. TSM does not use the 412-nm band; therefore, unlike the CHL results, all TSM data seem to have similar patterns and values although GOCI, G1-bicubic, and U-Net R_{rs} did not follow GOCI-II R_{rs} 555-nm pattern.

V. CONCLUSION

In this study, we developed a U-Net SR model to improve the spatial resolution of GOCI at 500 m to GOCI-II at 250 m. The R_{rs} data derived from our U-Net model can provide more spatial information than the original GOCI R_{rs} data about the optical properties of water in coastal areas, where the water features present fine-scale spatial dynamics. In addition, GOCI sensor degradation at the blue wavelength bands in the late mission period was noticeably improved, and accordingly, the overestimation tendency of the CHL product was also corrected. The accumulated GOCI over ten years since 2010 and the U-Net SR model can be utilized with GOCI-II for long-term monitoring. In other words, it is possible to derive a high-quality, consistent geostationary ocean color record at 250-m spatial resolution from 2010 to 2030. We believe that these data will enhance the understanding of ocean conditions around the waters of the Korean Peninsula.

REFERENCES

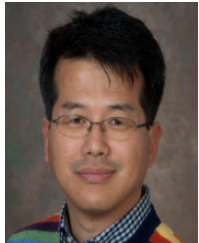
- [1] M.-S. Park, S. Lee, J.-H. Ahn, S.-J. Lee, J.-K. Choi, and J.-H. Ryu, “Decadal measurements of the first geostationary ocean color satellite (GOCI) compared with MODIS and VIIRS data,” *Remote Sens.*, vol. 14, no. 1, p. 72, Dec. 2021.
- [2] Y. B. Son and J.-K. Choi, “Mapping the Changjiang diluted water in the East China Sea during summer over a 10-year period using GOCI satellite sensor data,” *Frontiers Mar. Sci.*, vol. 9, Nov. 2022, Art. no. 1024306.
- [3] M. Xu, B. B. Barnes, C. Hu, P. R. Carlson, and L. A. Yarbro, “Water clarity monitoring in complex coastal environments: Leveraging seagrass light requirement toward more functional satellite ocean color algorithms,” *Remote Sens. Environ.*, vol. 286, Mar. 2023, Art. no. 113418.
- [4] J.-E. Min, J.-H. Ryu, S. Lee, and S. Son, “Monitoring of suspended sediment variation using Landsat and MODIS in the Saemangeum coastal area of Korea,” *Mar. Pollut. Bull.*, vol. 64, no. 2, pp. 382–390, Feb. 2012.
- [5] M. J. Behrenfeld et al., “Climate-driven trends in contemporary ocean productivity,” *Nature*, vol. 444, no. 7120, pp. 752–755, Dec. 2006.
- [6] D.-W. Kim, S.-H. Kim, and Y.-H. Jo, “Machine learning to identify three types of oceanic fronts associated with the Changjiang diluted water in the East China Sea between 1997 and 2021,” *Remote Sens.*, vol. 14, no. 15, p. 3574, Jul. 2022.
- [7] J. Shin, K. Kim, Y. Son, and J.-H. Ryu, “Synergistic effect of multi-sensor data on the detection of *Margalefidinium polykrikoides* in the South Sea of Korea,” *Remote Sens.*, vol. 11, no. 1, p. 36, Dec. 2018.
- [8] T. Zhou, Y. Li, B. Jiang, J. M. Alatalo, C. Li, and C. Ni, “Tracking spatio-temporal dynamics of harmful algal Blooms using long-term MODIS observations of Chaohu Lake in China from 2000 to 2021,” *Ecol. Indicators*, vol. 146, Feb. 2023, Art. no. 109842.
- [9] J. Shin, B.-K. Khim, L.-H. Jang, J. Lim, and Y.-H. Jo, “Convolutional neural network model for discrimination of harmful algal Bloom (HAB) from non-HABs using Sentinel-3 OLCI imagery,” *ISPRS J. Photogramm. Remote Sens.*, vol. 191, pp. 250–262, Sep. 2022.
- [10] K. Kim, J. Shin, K. Y. Kim, and J.-H. Ryu, “Long-term trend of green and golden tides in the Eastern Yellow Sea,” *J. Coastal Res.*, vol. 90, no. 1, pp. 317–323, Sep. 2019.

- [11] M. Wang and C. Hu, "Mapping and quantifying Sargassum distribution and coverage in the Central West Atlantic using MODIS observations," *Remote Sens. Environ.*, vol. 183, pp. 350–367, Jun. 2016.
- [12] J. Shin, J.-S. Lee, L.-H. Jang, J. Lim, B.-K. Khim, and Y.-H. Jo, "Sargassum detection using machine learning models: A case study with the first 6 months of GOCTO imagery," *Remote Sens.*, vol. 13, no. 23, p. 4844, Nov. 2021.
- [13] J.-H. Ryu, H.-J. Han, S. Cho, Y.-J. Park, and Y.-H. Ahn, "Overview of geostationary ocean color imager (GOCTO) and GOCTO data processing system (GDPS)," *Ocean Sci. J.*, vol. 47, no. 3, pp. 223–233, Sep. 2012.
- [14] J. Choi, Y. J. Park, J. H. Ahn, H. Lim, J. Eom, and J. Ryu, "GOCTO, the world's first geostationary ocean color observation satellite, for the monitoring of temporal variability in coastal water turbidity," *J. Geophys. Res., Oceans*, vol. 117, no. 9, pp. 2–12, Sep. 2012.
- [15] J. Eom et al., "Spatiotemporal variation in suspended sediment concentrations and related factors of coastal waters based on multispatial satellite data in Gyeonggi Bay, Korea," *J. Coastal Res.*, vol. 333, pp. 653–667, May 2017.
- [16] J. H. Noh, W. Kim, S. H. Son, J.-H. Ahn, and Y.-J. Park, "Remote quantification of *Cochlodinium polykrikoides* Blooms occurring in the East Sea using geostationary ocean color imager (GOCTO)," *Harmful Algae*, vol. 73, pp. 129–137, Mar. 2018.
- [17] J.-K. Choi et al., "Harmful algal Bloom (HAB) in the East Sea identified by the geostationary ocean color imager (GOCTO)," *Harmful Algae*, vol. 39, pp. 295–302, Oct. 2014.
- [18] X. Lou and C. Hu, "Diurnal changes of a harmful algal Bloom in the East China Sea: Observations from GOCTO," *Remote Sens. Environ.*, vol. 140, pp. 562–572, Jan. 2014.
- [19] Y. B. Son, B.-J. Choi, Y. H. Kim, and Y.-G. Park, "Tracing floating green algae Blooms in the Yellow Sea and the East China Sea using GOCTO satellite data and Lagrangian transport simulations," *Remote Sens. Environ.*, vol. 156, pp. 21–33, Jan. 2015.
- [20] J.-K. Choi, Y.-B. Son, M.-S. Park, D.-J. Hwang, J.-H. Ahn, and Y.-G. Park, "The applicability of the geostationary ocean color imager to the mapping of sea surface salinity in the East China Sea," *Remote Sens.*, vol. 13, no. 14, p. 2676, Jul. 2021.
- [21] M. Wang et al., "Ocean color products from the Korean Geostationary Ocean Color Imager (GOCTO)," *Opt. Exp.*, vol. 21, no. 3, pp. 3835–3849, 2013.
- [22] K.-A. Park, H.-J. Woo, and J.-H. Ryu, "Spatial scales of mesoscale eddies from GOCTO chlorophyll-A concentration images in the East/Japan Sea," *Ocean Sci. J.*, vol. 47, no. 3, pp. 347–358, Sep. 2012.
- [23] C. Donlon et al., "The global monitoring for environment and security (GMES) Sentinel-3 mission," *Remote Sens. Environ.*, vol. 120, pp. 37–57, May 2012.
- [24] A. Neckel et al., "Terrestrial nanoparticle contaminants and geospatial optics using the Sentinel-3B OLCI satellite in the Tinto River estuary region of the Iberian Peninsula," *Mar. Pollut. Bull.*, vol. 187, Feb. 2023, Art. no. 114525.
- [25] Z. Wang, J. Chen, and S. Hoi, "Deep learning for image super-resolution: A survey," *IEEE Trans. Pattern Anal. Mach. Intell.*, vol. 43, no. 10, pp. 3365–3387, Mar. 2020.
- [26] H. Greenspan, "Super-resolution in medical imaging," *Comput. J.*, vol. 52, no. 1, pp. 43–63, Jan. 2009.
- [27] J. S. Isaac and R. Kulkarni, "Super resolution techniques for medical image processing," in *Proc. Int. Conf. Technol. Sustain. Develop. (ICTSD)*, Feb. 2015, pp. 1–6.
- [28] L. Zhang, H. Zhang, H. Shen, and P. Li, "A super-resolution reconstruction algorithm for surveillance images," *Signal Process.*, vol. 90, no. 3, pp. 848–859, Mar. 2010.
- [29] Q. Wang, W. Shi, Z. Li, and P. M. Atkinson, "Fusion of Sentinel-2 images," *Remote Sens. Environ.*, vol. 187, pp. 241–252, Dec. 2016.
- [30] C. Dong, C. C. Loy, K. He, and X. Tang, "Image super-resolution using deep convolutional networks," *IEEE Trans. Pattern Anal. Mach. Intell.*, vol. 38, no. 2, pp. 295–307, Feb. 2016.
- [31] J. Kim, J. K. Lee, and K. M. Lee, "Deeply-recursive convolutional network for image super-resolution," in *Proc. IEEE Conf. Comput. Vis. Pattern Recognit. (CVPR)*, Jun. 2016, pp. 1637–1645.
- [32] J. Kim, J. K. Lee, and K. M. Lee, "Accurate image super-resolution using very deep convolutional networks," in *Proc. IEEE Conf. Comput. Vis. Pattern Recognit. (CVPR)*, Jun. 2016, pp. 1646–1654.
- [33] B. Lim, S. Son, H. Kim, S. Nah, and K. M. Lee, "Enhanced deep residual networks for single image super-resolution," in *Proc. IEEE Conf. Comput. Vis. Pattern Recognit. Workshops (CVPRW)*, Jul. 2017, pp. 136–144.
- [34] T. Zhang, H. Tang, Y. Ding, P. Li, C. Ji, and P. Xu, "FSRSS-Net: High-resolution mapping of buildings from middle-resolution satellite images using a super-resolution semantic segmentation network," *Remote Sens.*, vol. 13, no. 12, p. 2290, Jun. 2021.
- [35] T.-A. Teo and Y.-J. Fu, "Spatiotemporal fusion of Formosat-2 and Landsat-8 satellite images: A comparison of 'super resolution-then-blend' and 'blend-then-super resolution' approaches," *Remote Sens.*, vol. 13, no. 4, p. 606, Feb. 2021.
- [36] D. He and Y. Zhong, "Deep hierarchical pyramid network with high-frequency-aware differential architecture for super-resolution mapping," *IEEE Trans. Geosci. Remote Sens.*, vol. 61, 2023, Art. no. 5503815.
- [37] B. Cui, H. Zhang, W. Jing, H. Liu, and J. Cui, "SRSe-Net: Super-resolution-based semantic segmentation network for green tide extraction," *Remote Sens.*, vol. 14, no. 3, p. 710, Feb. 2022.
- [38] C. Lanaras, J. Bioucas-Dias, S. Galliani, E. Baltasavias, and K. Schindler, "Super-resolution of Sentinel-2 images: Learning a globally applicable deep neural network," *ISPRS J. Photogramm. Remote Sens.*, vol. 146, pp. 305–319, Dec. 2018.
- [39] X. Liu and M. Wang, "Super-resolution of VIIRS-measured ocean color products using deep convolutional neural network," *IEEE Trans. Geosci. Remote Sens.*, vol. 59, no. 1, pp. 114–127, Jan. 2021.
- [40] D. Doxaran et al., "Retrieval of the seawater reflectance for suspended solids monitoring in the East China Sea using MODIS, MERIS and GOCTO satellite data," *Remote Sens. Environ.*, vol. 146, pp. 36–48, Apr. 2014.
- [41] O. Ronneberger, P. Fischer, and T. Brox, "U-Net: Convolutional networks for biomedical image segmentation," in *Proc. Int. Conf. Med. Image Comput. Comput.-Assist. Intervent.*, 2015, pp. 234–241.
- [42] S. M. Kim, J. Shin, S. Baek, and J.-H. Ryu, "U-Net convolutional neural network model for deep red tide learning using GOCTO," *J. Coastal Res.*, vol. 90, no. 1, pp. 302–309, Sep. 2019.
- [43] J. Shin, Y.-H. Jo, J.-H. Ryu, B.-K. Khim, and S. M. Kim, "High spatial-resolution red tide detection in the Southern Coast of Korea using U-Net from PlanetScope imagery," *Sensors*, vol. 21, no. 13, p. 4447, Jun. 2021.
- [44] M. Wang and S. Son, "VIIRS-derived chlorophyll-A using the ocean color index method," *Remote Sens. Environ.*, vol. 182, pp. 141–149, Sep. 2016.
- [45] P. J. Brickley and A. C. Thomas, "Satellite-measured seasonal and inter-annual chlorophyll variability in the Northeast Pacific and coastal Gulf of Alaska," *Deep Sea Res. II, Topical Stud. Oceanogr.*, vol. 51, nos. 1–3, pp. 229–245, Jan. 2004.
- [46] K. Shi et al., "Long-term remote monitoring of total suspended matter concentration in Lake Taihu using 250 m MODIS-Aqua data," *Remote Sens. Environ.*, vol. 164, pp. 43–56, Jul. 2015.
- [47] Y. Zhang, K. Shi, Y. Zhou, X. Liu, and B. Qin, "Monitoring the river plume induced by heavy rainfall events in large, shallow, Lake Taihu using MODIS 250 m imagery," *Remote Sens. Environ.*, vol. 173, pp. 109–121, Feb. 2016.
- [48] J. E. O'Reilly et al., "Ocean color chlorophyll algorithms for SeaWiFS," *J. Geophys. Res., Oceans*, vol. 103, pp. 24937–24953, Oct. 1998.
- [49] J. E. Min, J. K. Choi, Y. J. Park, and J. H. Ryu, "Retrieval of suspended sediment concentration in the coastal waters of Yellow Sea from Geostationary Ocean Color Imager (GOCTO)," in *Proc. Int. Symp. Remote Sens.*, 2013, pp. 809–812.
- [50] C. Hu and C. Le, "Ocean color continuity from VIIRS measurements over Tampa Bay," *IEEE Geosci. Remote Sens. Lett.*, vol. 11, no. 5, pp. 945–949, May 2014.
- [51] W. Kim, J.-H. Ahn, and Y.-J. Park, "Correction of stray-light-driven intersensor radiometric discrepancy (ISRD) present in radiometric products of geostationary ocean color imager (GOCTO)," *IEEE Trans. Geosci. Remote Sens.*, vol. 53, no. 10, pp. 5458–5472, Oct. 2015.
- [52] C. S. Kim and H.-S. Lim, "Sediment dispersal and deposition due to sand mining in the coastal waters of Korea," *Continental Shelf Res.*, vol. 29, no. 1, pp. 194–204, Jan. 2009.
- [53] V. E. Brando, A. G. Dekker, A. Marks, Y. Qin, and K. Oubelkheir, "Chlorophyll and suspended sediment assessment in a macro-tidal tropical estuary adjacent to the great barrier reef: Spatial and temporal assessment using remote sensing," Cooperat. Res. Centre for Coastal Zone, Estuary Waterway Manage., Indooroopilly, QLD, USA, Tech. Rep. 74, 2006.
- [54] J. Eom, Y.-K. Lee, J.-K. Choi, J.-E. Moon, J.-H. Ryu, and J.-S. Won, "Monitoring of the suspended sediments concentration in Gyeonggi-Bay using COMS/GOCTO and Landsat ETM+ images," *Econ. Environ. Geol.*, vol. 47, no. 1, pp. 39–48, Feb. 2014.



Jisun Shin (Member, IEEE) received the M.S. degree in remote sensing from Yonsei University, Seoul, South Korea, in 2014, and the Ph.D. degree in ocean color from the National Korea Maritime and Ocean University, Busan, South Korea, in 2020.

She is currently a Post-Doctoral Researcher with the Department of Oceanography, Pusan National University, Busan. Her research interests include red, green, and golden tides, the use of seagrass for detection and prediction, and the related use of remote-sensing data and artificial intelligence techniques.



Young-Heon Jo received the master's degree from the Department of Oceanography, Florida State University, Tallahassee, FL, USA, in 1999, and the Ph.D. degree from the University of Delaware, Newark, DE, USA, in 2003.

Since then, he was with the Center for Remote Sensing, University of Delaware, as a Post-Doctoral Researcher, a Research Associate, and a Research Assistant Professor from 2003 to 2013. He has been a Professor with Pusan National University, Busan, South Korea, since 2013. His research interests include physical and dynamical oceanography and multi-satellite oceanography based on time series analysis, artificial intelligence, deep learning, and field remote-sensing observations.



Boo-Keun Khim received the Ph.D. degree in oceanography from the University of Delaware, Newark, DE, USA, in 1996.

He was a Post-Doctoral Researcher and a Senior Research Scientist with Seoul National University, Seoul, South Korea, from 1996 to 1998 and Korea Ocean Research and Development Institute, Ansan, South Korea, from 1998 to 2002. He has been a Professor with the Department of Oceanography, Pusan National University, Busan, South Korea, since 2002. His research interests include geological oceanography and paleoceanography using multiproxy of the deep-sea sediments in the global ocean.



Soo Mee Kim (Member, IEEE) received the Ph.D. degree in radiation and applied life science from Seoul National University, Seoul, South Korea, in 2010.

She was a Post-Doctoral Researcher of medical image processing with the Department of Nuclear Medicine, Seoul National University, from 2010 to 2012; the Department of Radiology, University of Washington, Washington, DC, USA, from 2012 to 2015; and the Division of Radiation Instrument Research, Korea Atomic Energy Research Institute, Daejeon, South Korea, from 2015 to 2017. Since 2017, she has been a Principal Research Scientist with the Maritime ICT and Mobility Research Department, Korea Institute of Ocean Science and Technology, Busan, South Korea. Her research interests include underwater sensing and signal-image processing for unmanned automation.